

Downward pumping of magnetic flux as the cause of filamentary structures in sunspot penumbrae

John H. Thomas*†, Nigel O. Weiss*, Steven M. Tobias‡ & Nicholas H. Brummell§

* Department of Applied Mathematics and Theoretical Physics, University of Cambridge, Cambridge CB3 0WA, UK

† Department of Physics and Astronomy and Department of Mechanical Engineering, University of Rochester, Rochester, New York 14627-0171, USA

‡ Department of Applied Mathematics, The University of Leeds, Leeds LS2 9JT, UK

§ JILA and Department of Astrophysical and Planetary Sciences, University of Colorado, Boulder, Colorado 80309-0440, USA

The structure of a sunspot is determined by the local interaction between magnetic fields and convection near the Sun's surface^{1,2}. The dark central umbra is surrounded by a filamentary penumbra, whose complicated fine structure has only recently been revealed by high-resolution observations^{3–14}. The penumbral magnetic field has an intricate and unexpected interlocking-comb structure and some field lines, with associated outflows of gas¹⁵, dive back down below the solar surface at the outer edge of the spot. These field lines might be expected to float quickly back to the surface because of magnetic buoyancy, but they remain submerged. Here we show that the field lines are kept submerged outside the spot by turbulent, compressible

convection, which is dominated by strong, coherent, descending plumes^{16,17}. Moreover, this downward pumping of magnetic flux explains the origin of the interlocking-comb structure of the penumbral magnetic field, and the behaviour of other magnetic features near the sunspot.

Near the solar surface there is a shallow, strongly superadiabatic layer with vigorous small-scale convection, lying over a weakly unstable region of gentler, larger-scale convection. The small-scale motion is responsible for the observed pattern of short-lived convection cells with diameters around 1,000 km (granules) at the solar surface, while the larger-scale motion manifests itself as supergranules with diameters around 30,000 km. We propose the picture of a sunspot shown in Fig. 1, in which granular convection plays a key role in submerging the returning penumbral flux tubes and establishing the structure of the penumbral magnetic field.

The basic ideas of convective pumping of magnetic flux may be traced back to earlier concepts (flux expulsion, turbulent diamagnetism, and topological pumping—see references in ref. 18). Recent numerical experiments have demonstrated that turbulent pumping of magnetic flux by penetrative convection at the base of the convection zone is an important ingredient of the dynamo that is responsible for cyclic activity in the Sun^{18–22}. These simulations of three-dimensional, compressible, turbulent convection have revealed the true dynamical nature of the pumping mechanism. The vigorous sinking plumes transport magnetic flux preferentially downwards out of the turbulent convecting region and into a stably stratified region below, where the flux can be amplified and stored. The calculations show that the pumping mechanism is remarkably robust, and works well even when the convective stability of the

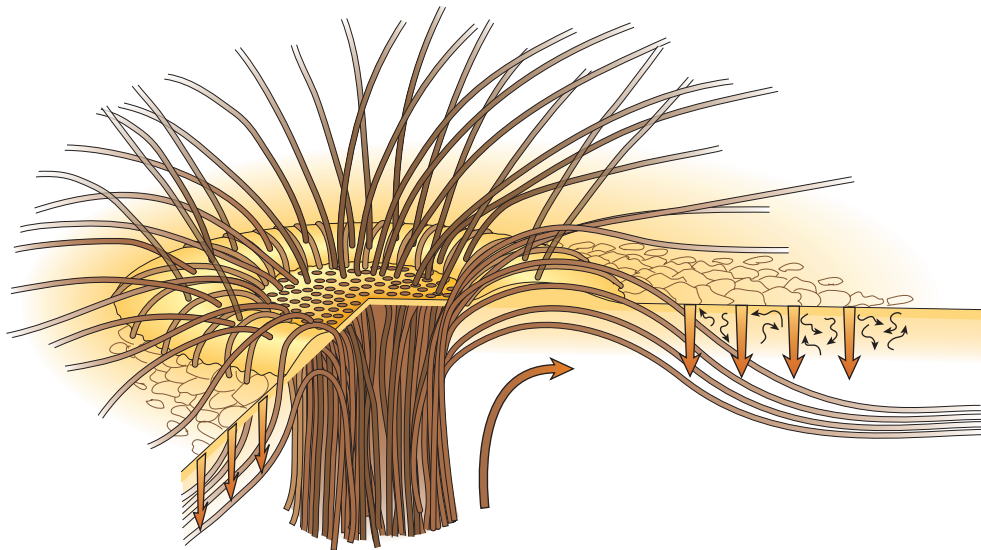


Figure 1 Sketch showing the interlocking-comb structure of the magnetic field in the filamentary penumbra of a sunspot. The bright radial filaments, where the magnetic field is inclined (at about 40° to the horizontal in the outer penumbra), alternate with dark filaments in which the field is nearly horizontal^{8,5–7,13}. Within the dark filaments, some magnetic flux tubes (that is, bundles of magnetic field lines) extend radially outward beyond the penumbra along an elevated magnetic canopy while other, 'returning' flux tubes dive back below the surface. The sunspot is surrounded by a layer of small-scale granular convection (thin squiggly black arrows) embedded in the radial outflow (thick curved brown arrow) associated with a long-lived annular supergranule (the moat cell). The submerged parts of the returning flux tubes are held down by turbulent pumping (indicated by thick vertical brown arrows) due to granular convection in the moat. There is also a persistent horizontal outflow in the penumbra (the Evershed flow), which is mostly

confined to thin, nearly horizontal, radial channels within the dark filaments. Because of the relatively high electrical conductivity of the gas, this flow is constrained to be along magnetic field lines. A small fraction of the flow runs along field lines that extend radially outward beyond the penumbral boundary along the magnetic canopy, elevated slightly above the surrounding quiet photosphere. Most of the Evershed flow, however, runs along arched magnetic flux tubes that dive back down below the visible surface at points either just within or just outside the outer boundary of the penumbra^{8–12}. This configuration is in close agreement with the siphon-flow model, in which a flow along an arched magnetic flux tube is driven by a drop in gas pressure between the two footpoints of the arch¹⁵; at the outer footpoint the intergranular magnetic field is stronger, the magnetic pressure is higher and the gas pressure is therefore lower.

lower layer is reduced¹⁸. We therefore expect that downward pumping by the granular convection just beneath the solar surface will be particularly effective.

To test the effects of flux pumping on sunspot structure, we have carried out calculations that are specifically designed to model turbulent pumping by granular convection. The model consists of a shallow, strongly superadiabatic layer representing the region where granules form, lying over a deep, nearly adiabatic layer representing the region of weaker, larger-scale (such as supergranular) motion. For computational reasons, the lower layer is in fact weakly stable, but this does not affect the qualitative features of the results. Figure 2 shows the initial and final states for this flux-pumping calculation. First, a purely hydrodynamic simulation with no magnetic field¹⁷ is carried out until a statistically steady state is reached. This steady state takes the form of vigorous, turbulent convection above a largely quiescent layer (Fig. 2a). The convection is dominated by a network of downflows, with the strongest flows in the downwards sinking plumes that penetrate into the layer below. Then, at time $t = 0$, we introduce into the fully developed convection a thin uniform layer of horizontal magnetic field $\mathbf{B} = (0, B_y, 0)$, as shown in Fig. 2b, and adjust the density of the layer so that the pressure remains continuous, although the magnetic slab is nearly evacuated and hence very buoyant.

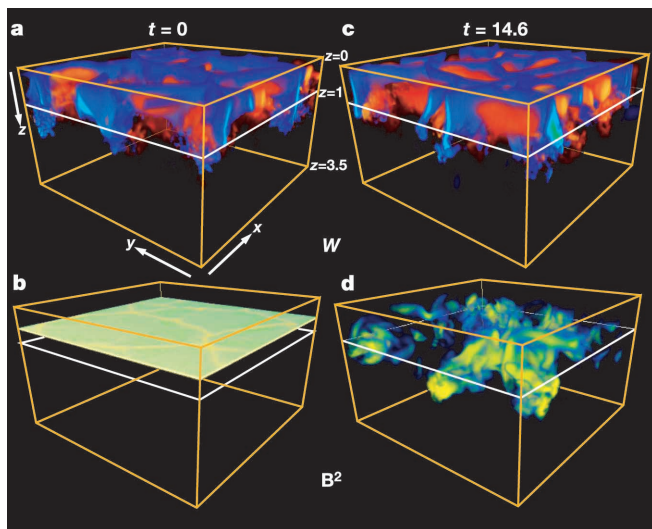


Figure 2 Downward pumping of magnetic flux by turbulent granular convection. Shown are volume renderings of the results of our numerical simulation, in a rectangular box of horizontal dimensions 6×6 and vertical dimension 3.5 in units of the depth of the upper ‘granulation’ layer. The vertical scale is exaggerated. The boundary conditions are periodic in the horizontal directions and stress-free at the top and bottom of the box; the magnetic field \mathbf{B} is constrained to be vertical at the upper boundary ($B_x = B_y = 0$ at $z = 0$) but no magnetic flux is allowed to escape across the bottom boundary ($\partial B_x / \partial z = \partial B_y / \partial z = 0$ at $z = 3.5$). The Rayleigh number $Ra = 5 \times 10^5$ and the initial field strength corresponds locally to a Chandrasekhar number $Q = 10^5$. The stiffness parameter $S = (m_2 - m_{ad}) / (m_{ad} - m_1)$, where m_1 and m_2 are the polytropic indices of the upper (unstable) and lower (stable) layer, respectively, and the adiabatic index $m_{ad} = 3/2$. Here we set $m_1 = 1$, $m_2 = 1.75$ so that $S = 0.5$. Other parameters are as in ref. 18, where the corresponding calculation had $S = 15$. **a**, Vertical velocity w of fully developed nonmagnetic convection at time $t = 0$, rendered with red/yellow indicating weak/strong upflows and blue/light blue indicating weak/strong downflows. **b**, The magnetic energy density just after the slab of uniform magnetic field (in the y direction) is introduced at $t = 0$. **c**, The vertical velocity after the pumping phase (at a dimensionless time $t = 14.6$). **d**, The magnetic energy density (increasing as blue–green–yellow) after the pumping phase. Strong coherent downflows penetrate from the ‘granular’ layer into the ‘supergranular’ layer below. These strong, sinking plumes amplify the magnetic energy locally, while pumping magnetic flux downward into the stable layer.

The magnetic field is immediately advected by the convection. Although some of the magnetic flux is transported upwards by the weaker upflows and magnetic buoyancy, and the upper boundary condition allows flux to leak through the surface, the strong downflows eventually overcome these effects and carry flux down towards the stable layer, amplifying the local magnetic energy as they plunge down. The velocity at the end of this pumping phase is shown in Fig. 2c, with the corresponding state of the magnetic energy shown in Fig. 2d. Although some magnetic flux remains within the convecting layer, a larger proportion has been swept down by the penetrating plumes into the layer below.

Three aspects of the final state are displayed in Fig. 3. The enstrophy (vorticity squared) is strongly concentrated in the vigorous sinking plumes at the corners of the network of downflows. These thin plumes splash down and broaden as they penetrate into the nearly adiabatic layer below. The field lines show the different field topologies in the stable and unstable regions. In the upper region, the plumes advect the tangled magnetic field, twisting and carrying it down into the nearly adiabatic layer to achieve the net transport downward of magnetic flux. In the lower region, the field is predominantly in the y direction, though the interaction with convection is still significant.

This downward transport is shown quantitatively in Fig. 4. In the initial pumping phase, the flux is transported predominantly by the action of convection. After an initial rise and loss of flux owing to magnetic buoyancy, efficient pumping of the magnetic flux takes over and the maximum of the flux appears in the nearly adiabatic layer (below $z = 1$). Although a significant mean flux remains in the turbulent layer, most of the net flux is in the stable region. This is the key feature of the computation—the downward transport of magnetic flux out of the layer of vigorous convection into the layer below. In the second phase of the calculation, flux drifts downward by diffusion (which would be a small factor in the Sun, but is significant in our model) and the flux profile diffuses deeper into the interior.

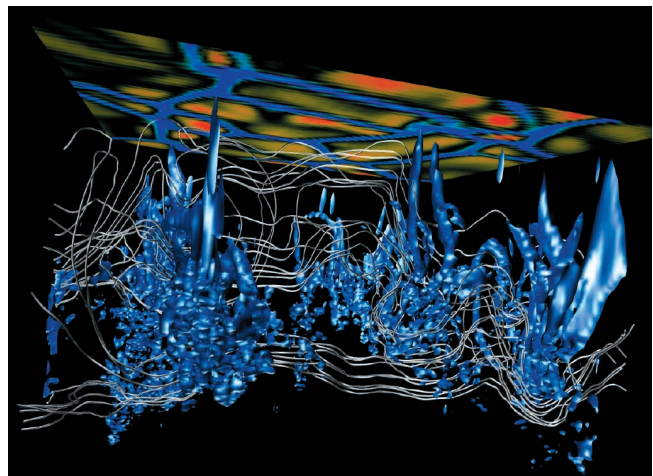


Figure 3 Flux pumping by vigorous sinking plumes. Perspective view from below the surface, showing an illuminated surface (in blue) of constant enstrophy density (that is, the square of the vorticity), which outlines the regions of strong descending plumes. At the top of the figure is a two-dimensional representation of the vertical velocity just below the surface, showing the small-scale convection as a network of downflows surrounding broad upflows, with yellow/red indicating weak/strong upflows, and light blue/blue indicating weak/strong downflows. The magnetic field is visualized by tracing selected bundles of representative field lines, some in the upper ‘granulation’ layer and some in the slightly stable, nearly adiabatic layer below. Note that these field lines correspond to different field strengths, and give no indication of the strength of the field. The tangled field in the upper region is pumped downwards into the stably stratified layer, where the field is predominantly in the y direction.

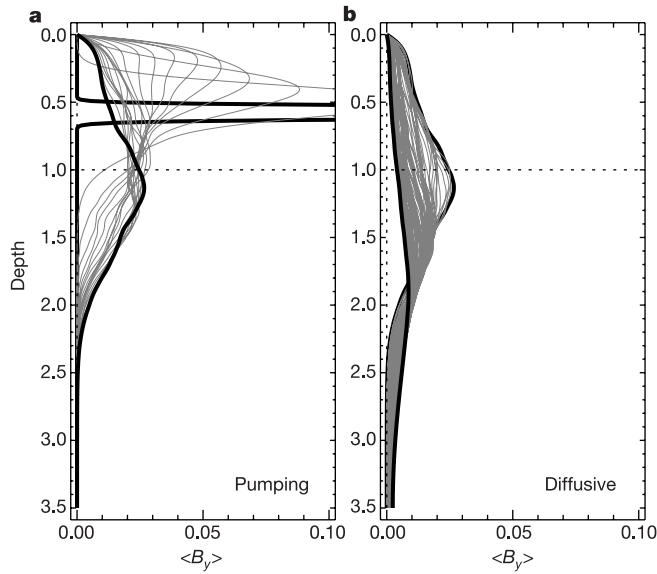


Figure 4 Downward pumping of magnetic flux in the numerical simulation. Plots show the horizontal average of the y -component of the magnetic field as a function of depth z at evenly spaced times, for two phases of the calculation. Panel **a** shows the rapid pumping phase ($0 \leq t \leq 9$), in which redistribution of the field occurs mainly as a result of the convective motions, and panel **b** shows the later slow diffusive phase, in which magnetic diffusion is the main transport mechanism. Heavy lines denote the flux distributions at the beginning and end of each phase. At first magnetic flux moves upwards, owing to magnetic buoyancy, and some leaks out through the upper boundary. Then the mean field is rapidly pumped downwards into the weakly stable region. Note, however, that a strong tangled field still survives in the vigorously convecting layer. The normalized field strength B can be related to the local gas pressure in the original static atmosphere by introducing the plasma β (the ratio of gas pressure to magnetic pressure): at $z = 0.5$, $\beta \approx 14/B^2$, while at $z = 1.0$, $\beta \approx 48/B^2$.

Overall, this simulation implies that the vigorously convecting granulation layer at the solar surface is very effective at expelling magnetic flux and pumping some of this flux into the underlying layer of gentler supergranular and larger-scale flows, where magnetic buoyancy becomes relatively more powerful. This in turn implies that flux pumping is an important mechanism for the formation and maintenance of a sunspot penumbra. A sunspot forms through the coalescence of small pores without penumbrae. As the total magnetic flux in a pore increases, the force balance demands that the outermost magnetic field lines become more nearly horizontal. When these field lines reach some critical angle, a convectively driven filamentary instability sets in^{23–25}. The resultant fluting at the boundary brings some of the outermost field lines down to the surface, where they can be grabbed and pumped downwards by granular convection. The nonlinear development of this process then leads to the formation of the penumbra, with its interlocking-comb field. This instability is subcritical, giving rise to hysteresis. As a sunspot decays, the pumping keeps most of these field lines submerged, thus explaining the existence of spots (with penumbrae) that contain less magnetic flux than the largest pores.

The submergence of some of the penumbral magnetic flux by convective pumping also explains the behaviour of the moving magnetic features (MMFs) that travel radially outward across the sunspot moat. The MMFs may be divided into three types²⁶ (Fig. 5). Type I MMFs have been interpreted as the footpoints of magnetic loops popping up from a submerged, horizontal flux sheet²⁷. As such, they fit well into our picture of flux that is held down by granular pumping, as we would expect short loops of flux to be occasionally brought to the surface by rising convective plumes. Type III MMFs would occur if the pumping mechanism occasion-

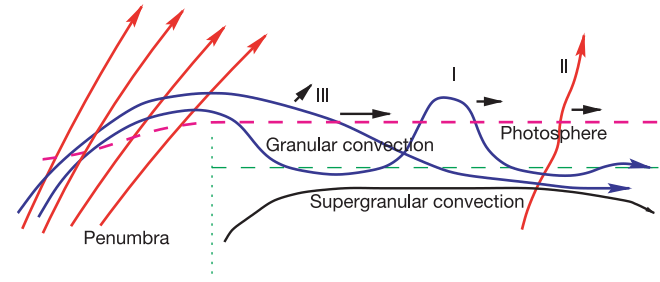


Figure 5 Moving magnetic features (MMFs) in the moat around a sunspot. Representative magnetic field lines of both the inclined magnetic field (red) in the bright filaments and the nearly horizontal magnetic field (blue) in the dark filaments are displayed. The sketch shows the configuration of MMFs of three types (I, II, III), interpreted in terms of magnetic flux pumping by granular convection in the sunspot moat. Type I MMFs are bipolar pairs of magnetic footpoints moving outward together at speeds of $0.5\text{--}1\text{ km s}^{-1}$, with the inner footpoint usually having the same polarity as the spot. Type II MMFs are single footpoints, with the same polarity as the sunspot, moving outward across the moat at speeds similar to that of type I MMFs. Type III MMFs are single footpoints with polarity opposite that of the sunspot that move rapidly outward at speeds of $2\text{--}3\text{ km s}^{-1}$.

ally allows an entire submerged penumbral flux tube to rise buoyantly and emerge through the surface at a shallow angle to the horizontal, producing a rapid outward motion of the footpoint across the moat. Type II MMFs are associated with flux tubes peeling off the sunspot and being transported horizontally outward by convection; they cause a loss of magnetic flux and decay of the sunspot. □

Received 22 May; accepted 3 October 2002; doi:10.1038/nature01174.

1. Thomas, J. H. & Weiss, N. O. (eds) *Sunspots: Theory and Observations* NATO ASI C. 375 (Kluwer, Dordrecht, 1992).
2. Schmieder, B., del Toro Iniesta, J. C. & Vázquez, M. (eds) *Advances in the Physics of Sunspots* Astronomical Society of the Pacific Conference Series 118, (San Francisco, 1997).
3. Degenhardt, D. & Wiehr, E. Spatial variation of the magnetic field inclination in a sunspot penumbra. *Astron. Astrophys.* **252**, 821–826 (1991).
4. Solanki, S. K. & Montavon, C. A. P. Uncombed fields as the source of broad-band circular polarization of sunspots. *Astron. Astrophys.* **275**, 283–292 (1993).
5. Title, A. M. et al. On the magnetic and velocity field geometry of simple sunspots. *Astrophys. J.* **403**, 780–796 (1993).
6. Lites, B. W., Elmore, D. F., Seagraves, P. & Skumanich, A. Stokes profile analysis and vector magnetic fields. VI. Fine-scale structure of a sunspot. *Astrophys. J.* **418**, 928–942 (1993).
7. Solanki, S. K., Montavon, C. A. P. & Livingston, W. Infrared lines as a probe of solar magnetic features. VII. On the nature of the Evershed effect in sunspots. *Astron. Astrophys.* **283**, 221–231 (1994).
8. Rimmele, T. R. Sun center observations of the Evershed effect. *Astrophys. J.* **445**, 511–516 (1995).
9. Stanchfield, D. C. H. II, Thomas, J. H. & Lites, B. W. The vector magnetic field, Evershed flow, and intensity in a sunspot. *Astrophys. J.* **477**, 485–494 (1997).
10. Westendorp Plaza, C. et al. Evidence for a downward mass flux in the penumbral region of a sunspot. *Nature* **389**, 47–49 (1997).
11. Rüedi, I., Solanki, S. K. & Keller, C. U. Infrared lines as probes of solar magnetic features. XV. Evershed flow in cool, weak penumbral fields. *Astron. Astrophys.* **348**, L37–L40 (1999).
12. Schlichenmaier, R. & Schmidt, W. Flow geometry in a sunspot penumbra. *Astron. Astrophys.* **358**, 1122–1132 (2000).
13. Martínez Pillet, V. Spectral signature of uncombed magnetic fields. *Astron. Astrophys.* **361**, 734–742 (2000).
14. Westendorp Plaza, C., del Toro Iniesta, J. C., Ruiz Cobo, B. & Martínez Pillet, V. Optical tomography of a sunspot. III. Velocity stratification and the Evershed effect. *Astrophys. J.* **547**, 1148–1158 (2001).
15. Montesinos, B. & Thomas, J. H. The Evershed effect in sunspots as a siphon flow along a magnetic flux tube. *Nature* **390**, 485–487 (1997).
16. Stein, R. F. & Nordlund, Å. Simulations of solar granulation. I. General properties. *Astrophys. J.* **499**, 914–933 (1998).
17. Brummell, N. H., Clune, T. L. & Toomre, J. Penetration and overshooting in turbulent compressible convection. *Astrophys. J.* **570**, 825–854 (2002).
18. Tobias, S. M., Brummell, N. H., Clune, T. L. & Toomre, J. Transport and storage of magnetic field by overshooting turbulent compressible convection. *Astrophys. J.* **549**, 1183–1203 (2001).
19. Nordlund, Å. et al. Dynamo action in stratified convection with overshoot. *Astrophys. J.* **392**, 647–652 (1992).
20. Brandenburg, A. et al. Magnetic structures in a dynamo simulation. *J. Fluid Mech.* **306**, 325–352 (1996).
21. Tobias, S. M., Brummell, N. H., Clune, T. L. & Toomre, J. Pumping of magnetic fields by turbulent penetrative convection. *Astrophys. J.* **502**, L177–L180 (1998).
22. Dorc, S. B. F. & Nordlund, Å. On the transport of magnetic fields by solar-like stratified convection. *Astron. Astrophys.* **365**, 562–570 (2001).
23. Rucklidge, A. M., Schmidt, H. U. & Weiss, N. O. The abrupt development of penumbrae in sunspots. *Mon. Not. R. Astron. Soc.* **273**, 491–498 (1995).

24. Schlichenmaier, R., Jahn, K. & Schmidt, H. U. A dynamical model for the penumbral fine structure and the Evershed effect in sunspots. *Astrophys. J.* **493**, L121–L124 (1998).
25. Tildesley, M. J. On the origin of filamentary structure in sunspot penumbrae: Linear instabilities. *Mon. Not. R. Astron. Soc.* (submitted).
26. Shine, R. A. & Title, A. M. in *Encyclopedia of Astronomy and Astrophysics* (Nature Publishing Group, London and Institute of Physics Publishing, Bristol, 2001).
27. Harvey, J. & Harvey, K. Observations of moving magnetic features near sunspots. *Sol. Phys.* **28**, 61–71 (1973).

Acknowledgements We thank J. Kuwabara and Y. Uchida for assistance in producing Fig. 3. This work was supported by the UK Particle Physics and Astrophysics Research Council (J.H.T. and N.O.W.), the Sun–Earth Connection Theory programme of the US National Aeronautics and Space Administration (N.H.B. and S.M.T.), and the Nuffield Foundation (S.M.T.).

Competing interests statement The authors declare that they have no competing financial interests.

Correspondence and requests for materials should be addressed to J.H.T. (e-mail: thomas@me.rochester.edu).

High brightness electron beam from a multi-walled carbon nanotube

Niels de Jonge*, Yann Lamy*†, Koen Schoots*‡ & Tjerk H. Oosterkamp‡

* Philips Research Laboratories, Prof. Holstlaan 4, 5656 AA Eindhoven, The Netherlands

† Ecole Supérieure de Physique et de Chimie Industrielles de la ville de Paris, 10 Rue Vauquelin, 75005 Paris, France

‡ Leiden Institute of Physics, Niels Bohrweg 2, 2333 CA Leiden, The Netherlands

Carbon nanotubes can act as electron sources¹ with very rigid structures², making them particularly interesting for use as point electron sources in high-resolution electron-beam instruments. Promising results have been reported with respect to some important requirements for such applications: a stable emitted current^{3,4,5} and a long lifetime^{6,7}. Two parameters of an electron source affect the resolution of these instruments: the energy spread of the emitted electrons and a parameter called the reduced brightness, which depends on the angular current density and the virtual source size. Several authors have measured a low energy spread associated with electron emission^{3,7,8,9}. Here we measure the reduced brightness, and find a value that is more than a factor of ten larger than provided by state-of-the-art electron sources in electron microscopes. In addition, we show that an individual multi-walled carbon nanotube emits most current into a single narrow beam. On the basis of these results, we expect that carbon nanotube electron sources will lead to a significant improvement in the performance of high-resolution electron-beam instruments.

The experiments were carried out with individual multi-walled carbon nanotubes mounted on tungsten tips. Figure 1 shows the transmission electron microscopy (TEM) images of a carbon nanotube with a geometrical radius of the tube apex of 2.7 nm. As can be seen in Fig. 1b, the nanotube had a closed capping. The formation of a small probe in an electron microscope requires a small virtual source. The virtual source is the area the electrons appear to originate from when their trajectories are traced back and is usually smaller than the real emitting surface of the source¹⁰.

To determine the virtual source size, the nanotube of Fig. 1 was mounted as electron source in a point projection electron microscope in an ultrahigh vacuum system with a base pressure of 2×10^{-10} torr (ref. 11). In this setup (Fig. 2a), the emitter is positioned at a small distance (a few micrometres), z_1 , from a sharp edge provided by one of the holes in the carbon film of a TEM grid. Electrons emitted by the source generate an image on the

screen at a distance $z_2 = 16$ cm (the magnification is given by $M = z_2/z_1$). For a sufficiently small virtual source and a sufficiently sharp edge, this image shows a Fresnel interference pattern. Figure 2b shows the image of a hole in the carbon film with a clearly visible fringe pattern. A line scan across the fringes was made in a direction parallel to the long side of the rectangle drawn in the fringe pattern and plotted in Fig. 2c. A total of eight fringes was visible, using the criterion that a fringe is considered to be visible when its amplitude is not smaller than one-tenth of the amplitude of the first fringe.

The position of the n th maximum $x(n)$ with respect to the first maximum $x(0)$ in the Fresnel fringe pattern can be expressed by¹²:

$$x(n) - x(0) = z_2 \sqrt{\frac{2\lambda}{z_1}} \left(\sqrt{n + \frac{3}{8}} - \sqrt{\frac{3}{8}} \right) \quad (1)$$

where

$$x(0) = z_2 \sqrt{\frac{2\lambda}{z_1}} \frac{3}{8} \quad (2)$$

with λ the electron wavelength. The width of the fringes decreases with increasing fringe number. Equation (1) was fitted to the experimental values of the positions of the maxima as determined from the line scan (Fig. 2c) and resulted in a value of z_1 of $3.9 \mu\text{m}$ (thus the magnification $M = 4.1 \times 10^4$). The differences between the experimental values of the positions of the maxima and the positions that followed from this fit were less than 8%.

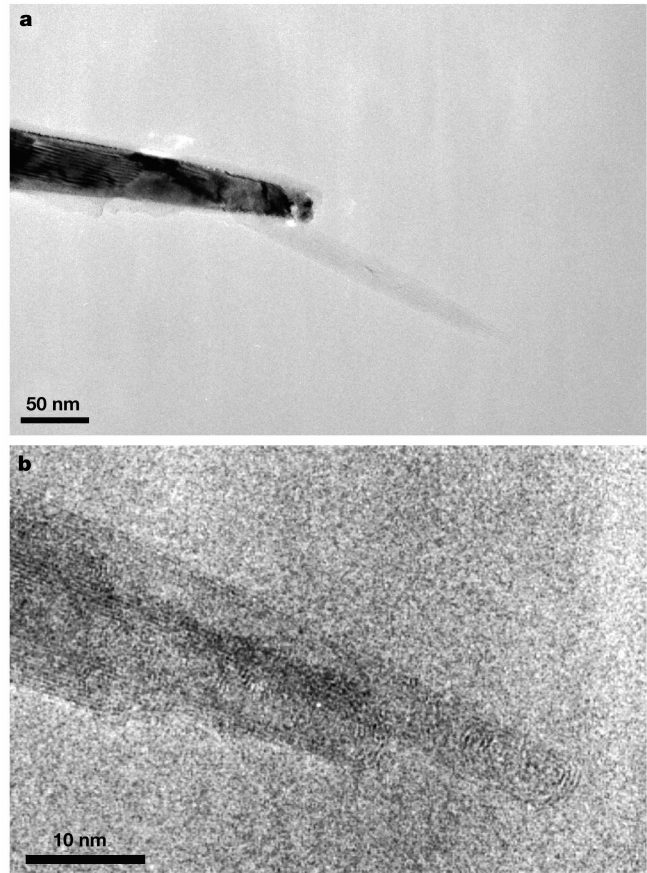


Figure 1 Transmission electron microscopy (TEM) images of an individual multi-walled carbon nanotube mounted on a tungsten tip. In **a**, the whole nanotube and the end of the tungsten tip can be seen. The glue from the carbon tape, which was used to fix the nanotube, is also visible. **b**, High-resolution TEM image of the apex of the tube with a radius of 2.7 nm.